Modeling of Microsegregation in Macrosegregation Computations

H. COMBEAU, J.-M. DREZET, A. MO, and M. RAPPAZ

A general framework for the calculation of micro-macrosegregation during solidification of metallic alloys is presented. In particular, the problems of back diffusion in the primary solid phase, of eutectic precipitation at the end of solidification, and of remelting are being addressed for an open system, *i.e.*, for a small-volume element whose overall solute content is not necessarily constant. Assuming that the variations of enthalpy and of solute content are known from the solution of the macroscopic continuity equations, a model is derived which allows for the calculation of the local solidification path (*i.e.*, cooling curve, volume fraction of solid, and concentrations in the liquid and solid phases). This general framework encompasses four microsegregation models for the diffusion in the solid phase: (1) an approximate solution based upon an internal variable approach; (2) a modification of this based upon a power-law approximation of the solute profile; (3) an approach which approximates the solute profile in the primary phase by a cubic function; and (4) a numerical solution of the diffusion equation based upon a coordinate transformation. These methods are described and compared for several situations, including solidification/remelting of a closed/open volume element whose enthalpy and solute content histories are known functions of time. It is shown that the solidification path calculated with method 2 is more accurate than using method 1, and that 2 is a very good approximation in macrosegregation calculations. Furthermore, it is shown that method 3 is almost identical to that obtained with a numerical solution of the diffusion equation (method 4). Although the presented results pertain to a simple binary alloy, the framework is general and can be extended to multicomponent systems.

I. INTRODUCTION

MATHEMATICAL computations of macrosegregation development during alloy solidification has received increasing interest during recent years.[1–13] Central to such computations is a model relating the specific enthalpy and local average solute concentration to the solid fraction, temperature, and solute concentrations in the solid and liquid parts of the two-phase volume elements, *i.e.*, a description of the local solidification path. Many computations so far have been based upon the lever rule approximation, *i.e.*, upon the assumption of local complete mixing of solute in the solid and liquid phases. However, the Scheil approximation, which is based upon the assumptions of complete solute redistribution locally in the liquid, of no solid diffusion, and of thermodynamic equilibrium at the solid-liquid interface, constitutes a better description of solidification than the lever rule for most alloys. Often, even more elaborate models accounting for finite diffusion in the solid dendrites[14–28] are needed, particularly if eutectic distributions and/or shrinkage-induced flows are of interest.[29] Except for the models in References 26 through 28, there are three main problems related to the use of nonequilibrium solidification descriptions.

(1) The approximative analytical expressions accounting for finite solute diffusion in the solid[14–18] rely on a simplified presumption concerning the dendritic growth kinetics, which does not necessarily apply for an industrial casting situation. For example, the conditions of so-called parabolic solidification is not met in aluminium d.c. casting where local remelting occurs due to complex boundary conditions.[11,12,30–32]
(2) The analytical expressions in References 14 through 18 are all based upon the assumption of a constant average concentration within the considered volume element (*i.e.*, closed system). This assumption cannot be made in macrosegregation computations since the prediction of changes in the local average concentration requires the consideration of an open system.
(3) Accounting for remelting in situations in which changes in average concentration and/or finite solute diffusion in the dendrites occur requires that the solute concentration in the dendritic structure during solidification be traced.[33,34] In other words, transport phenomena at two different scales have to be dealt with: the macro scale of the casting and the micro scale of the dendrites.

While the situation of no microscale diffusion (*i.e.*, Scheil approximation) can be handled in macrosegregation computations by a tracing method,[3,8,35–37] finite, nonzero diffusion requires a solution of Fick's second law for an appropriate microstructural morphology.[20–25] A simplification of this two-scale problem has been proposed by Wang and Beckermann.[26,27] Their method is based upon an approximation for the diffusion length in the dendrites. Another method was recently proposed by Mo,[28] who accounted for the effect of the microscopic solute diffusion

H. COMBEAU, Assistant Professor, is with the Laboratoire de Science et Génie des Materiaux Metallique, INPL, Ecole des Mines de Nancy, F-54042 Nancy, Cedex, France. J.-M. DREZET, Postdoctoral fellow, is with the Laboratoire de Métallurgie Physique, Ecole Polytechnique Fédérale de Lausanne, CH-1015 Lausanne, Switzerland. M. RAPPAZ, Professor, is with the Department des Materiaux, Ecole Polytechnique Fédérale de Lausanne, MX-G, CH-1015 Lausanne. A. MO, PhD, Senior Scientist, is with SINTEF Materials Technology, N-0314 Oslo, Norway.

Manuscript submitted August 3, 1995.

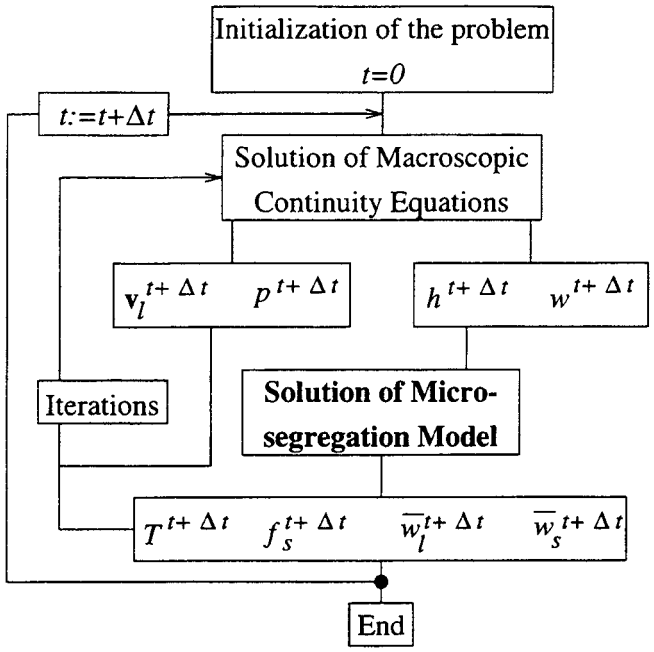

Fig. 1—Flow chart of a micro-macrosegregation calculation.

in the solid by regarding the concentrations of the alloying elements in the solid as so-called internal variables for which evolution equations were derived.

The purpose of the present article is to review various approaches of microsegregation models which can be implemented in macrosegregation computations and to compare these methods in case studies. The formal mathematical structure of micro-macrosegregation computations and the main ideas behind the internal variable method[28] are summarized in Section II. A modification of the internal variable model based upon a power-law approximation of the solute profile in the dendrites and the similarities between this model and the approach in References 26 and 27 are also presented, and the power-law approximation is extended to encompass various microstructural morphologies. An approximate methodology applying a collocation method and the exact diffusion problem are then presented. The algorithm for incorporation of the solidification path models in macrosegregation computations is presented in Section III, and particular attention is paid to the treatment of a eutectic reaction at the end of solidification. Also, the numerical solution of Fick's second law in a one-dimensional platelike secondary dendrite arm is presented. Section IV is devoted to case studies reflecting solidification of a closed system as well as possible remelting and variation of the overall solute content that can occur during the solidification of a binary alloy. Finally, in Section V, some of the main assumptions on which the present investigation has been based are discussed.

II. THEORETICAL FRAMEWORK

A. *Mathematical Structure of Micro-Macrosegregation Computations*

The goal of macrosegregation computations is to predict solute concentration inhomogeneities at the scale of a whole casting. Such calculations encompass the resolution of the averaged continuity equations at the macroscopic scale (Figure 1). Using known entities at time t, the average velocity of the fluid, $\mathbf{v}_l^{t+\Delta t}$, the local pressure, $p^{t+\Delta t}$, the specific enthalpy, $h^{t+\Delta t}$, and the average local solute concentration, $w^{t+\Delta t}$ at the next time-step thus can be deduced at some points of an enmeshment.* In the solidification interval, a microsegregation model is needed in order to deduce the local solidification path of the alloy from the known variations of enthalpy and average solute concentrations. As such, the micromodel can predict the new temperature, $T^{t+\Delta t}$, mass fraction of solid, $f_s^{t+\Delta t}$, average solute concentration in the liquid, $\overline{w}_l^{t+\Delta t}$, and average solute concentration in the solid, $\overline{w}_s^{t+\Delta t}$. In the present investigation, emphasis is placed on the micromodel, assuming that $h(t)$ and $w(t)$ are known functions of time which could result from the solution of the macroscopic continuity equations (Figure 1).

*For the sake of simplicity, binary alloys will be considered here. The average solute concentration and enthalpy of a small volume element will be simply noted w and h (instead of $\overline{w}$ and $\overline{h}$).

Assuming constant thermophysical properties and equal densities of the liquid and solid phases, the specific enthalpy is related to the solid mass fraction and the temperature by

$$h = c_p T + L(1 - f_s) \quad [1]$$

where c_p and L are the specific heat capacity and latent heat of fusion, respectively. Furthermore, assuming the material to be free of pores, the average solute concentration for a binary alloy is related to f_s, $\overline{w}_l$, and $\overline{w}_s$ by

$$w = (1 - f_s)\overline{w}_l + f_s\overline{w}_s \quad [2]$$

The simplest form of constitutive solidification equations is the lever rule approximation. Assuming constant liquidus slope, m, and partition coefficient, k, the lever rule can mathematically be expressed as

$$T = T_m + m\overline{w}_l \quad [3]$$

$$\overline{w}_s = k\overline{w}_l \quad [4]$$

where T_m is the melting temperature. Combined with Eqs. [1] and [2], these two equations yield f_s, T, $\overline{w}_l$, and $\overline{w}_s$ for given values of w and h between the liquidus temperature and the eutectic temperature.

The assumption of complete solute redistribution in the liquid is kept in what follows, and thermodynamic equilibrium at the solid-liquid interface is imposed. However, the assumption of complete solute redistribution in the solidified dendrites being relaxed, Eq. [4] is only valid for the solute concentration in the solid at the interface, w_s^*:

$$w_s^* = k\overline{w}_l \quad [5]$$

Generally, the superscript * refers to quantities at the solid-liquid interface.

B. *The Internal Variable Model*

Instead of linking $\overline{w}_s$ to $\overline{w}_l$ *via* Eq. [4], $\overline{w}_s$ is considered as an internal variable which will change due to solidification, remelting, and solute diffusion in the dendrites. This microstructure development is to be quantified by an ordinary differential equation (ODE) relating $d\overline{w}_s/dt$ to macroscopically defined quantities. As described in more detail

in References 28 and 34, time derivation of $f_s\overline{w}_s$ and Leibniz' rule are applied, and equilibrium is imposed at the solid-liquid interface (*cf.* Eq. [5]). Fick's second law for diffusion in platelike secondary dendrite arms then gives

$$\frac{d\overline{w}_s}{dt} = \left(\frac{k\overline{w}_l - \overline{w}_s}{f_s}\right)\frac{df_s}{dt} + \frac{1}{f_s}\frac{D_s}{x_0^2}\frac{\partial w_s^*}{\partial \eta} \qquad [6]$$

Here, t is time, η is a dimensionless variable normalized with respect to half of the characteristic secondary dendrite arm spacing, x_0, $w_s(\eta)$ is the solute concentration in the dendrite arm, and D_s is the solute diffusivity in the solid.

With Eq. [6] as a starting point, an evolution equation for $\overline{w}_s$ can be derived, as described in Reference 28. First, the solute flux at the interface is assumed to be proportional to the difference between the interfacial value of the solute concentration and the averaged solute concentration in the solid phase. Second, it is pointed out that the lever rule limit can be associated with the largest possible interfacial flux during solidification or remelting and that the interfacial flux in this limit is proportional to $[1 - (1 - k)f_s]^{-1}$. These two considerations lead to the approximative evolution equation

$$\frac{d\overline{w}_s}{dt} = \frac{k\overline{w}_l - \overline{w}_s}{f_s}\left[\frac{df_s}{dt} + \frac{D_s}{x_0^2}\frac{\xi}{1 - (1 - k)f_s}\right] \qquad [7]$$

where ξ is an adjustable parameter. It should be noted that such empirical constants are normally introduced in internal variable equations in order to fit experimental data (for example, Reference 38).

As pointed out in Reference 33, the special cases of constant w (closed system) and of solidification solely (no remelting) can be modeled by the Scheil approximation without any need to trace the solute concentration in the dendrites during solidification. This is equivalent to setting $D_s = 0$ in Eq. [7]. Furthermore, the evolution equation reveals that the lever rule is a limiting case. Since, for $D_s \to \infty$, the factor multiplying the right-hand-side bracket must tend toward zero, *i.e.*, $\overline{w}_s = k\overline{w}_l$.

C. *Power-Law Approximation*

A different evolution equation can be derived by assuming a particular approximation for the solute profile in the platelike secondary dendrite arm. For example, a minor modification of Ohnaka's[16] parabolic profile is

$$w_s(\eta) = a\eta^\gamma + b \qquad [8]$$

which fulfill the symmetry requirement $\partial w_s/\partial\eta = 0$ at $\eta = 0$ if $\gamma > 1$. The constants a and b can be related to $\overline{w}_s$ and $\overline{w}_l$ by the definition

$$\overline{w}_s = \frac{1}{f_s}\int_0^{f_s(t)} w_s(\eta)d\eta \qquad [9]$$

and the interfacial equilibrium assumption represented by Eq. [5]. Hence, it can be shown that

$$\frac{\partial w_s^*}{\partial \eta} = (\gamma + 1)\frac{k\overline{w}_l - \overline{w}_s}{f_s} \qquad [10]$$

which inserted into Eq. [6] yields

$$\frac{d\overline{w}_s}{dt} = \frac{k\overline{w}_l - \overline{w}_s}{f_s}\left[\frac{df_s}{dt} + \frac{D_s(\gamma + 1)}{x_0^2}\frac{}{f_s}\right] \qquad [11]$$

This evolution equation can be regarded as a modification of Eq. [7] in that the denominator $[1 - (1 - k)f_s]$ has been interchanged with f_s. The constant γ determining the form of the solute profile plays the role of an adjustable parameter. In what follows, the model will be referred to as the *power-law approximation*, while the model based upon Eq. [7] will be referred to as the *internal variable approach.*

It should be noted that the solidification equation outlined by Wang and Beckermann (Reference 26, Eq. [2]) reduces to Eq. [11] if total solute redistribution in the liquid and solid-liquid interface equilibrium are assumed. Central to their derivation is an approximation for the diffusion length based upon the assumption of a parabolic solute profile, *i.e.*, γ is equal to 2. Wang and Beckermann[26,27] demonstrated that their model is a good approximation when parabolic solidification is considered. However, they did not investigate the performance of the model in situations in which remelting and/or changes in total solute concentration occur.

D. *Microstructure Morphology*

While Eq. [11] has been derived for a platelike secondary dendrite arm morphology, the secondary arms of well-developed columnar and equiaxed dendritic microstructures are better approximated by cylindrical geometries than by a platelike morphology. Globulitic structures typical of heavily inoculated aluminum alloys can be fairly well approximated by spherical geometries. For such situations, it can be shown that Eq. [6] is changed to

$$\frac{d\overline{w}_s}{dt} = \left(\frac{k\overline{w}_l - \overline{w}_s}{f_s}\right)\frac{df_s}{dt} + \frac{4D_s}{x_0^2}\cdot\frac{\partial w_s^*}{\partial \eta} \quad \text{(cylindrical)} \qquad [12]$$

and

$$\frac{d\overline{w}_s}{dt} = \left(\frac{k\overline{w}_l - \overline{w}_s}{f_s}\right)\frac{df_s}{dt} + \frac{9D_s}{x_0^2}\cdot f_s^{1/3}\cdot\frac{\partial w_s^*}{\partial \eta} \quad \text{(spherical)} \qquad [13]$$

The dimensionless variable η is normalized with respect to the square of the cylinder radius, $\eta = (x/x_0)^2$, and the cube of the sphere radius, $\eta = (x/x_0)^3$, respectively, where x_0 is the radius of the elementary volume element. These normalizations of η are made in such a way that the definition of the average concentration (Eq. [9]) remains unchanged for the spherical and cylindrical geometries. Using the same power-law approximation for the solute profile (Eq. [8]), the following evolution equations are obtained:

$$\frac{d\overline{w}_s}{dt} = \frac{k\overline{w}_l - \overline{w}_s}{f_s}\left[\frac{df_s}{dt} + \frac{4D_s}{x_0^2}(\gamma + 1)\right] \quad \text{(cylindrical)} \qquad [14]$$

and

$$\frac{d\overline{w}_s}{dt} = \frac{k\overline{w}_l - \overline{w}_s}{f_s}\left[\frac{df_s}{dt} + \frac{9D_s}{x_0^2}f_s^{1/3}(\gamma + 1)\right] \quad \text{(spherical)} \qquad [15]$$

Please note that with the normalization of η, a parabolic solute profile in the platelike, cylindrical, and spherical geometries is given by $\gamma = 2$, $\gamma = 1$, and $\gamma = 2/3$, respectively.

The evolution equations for the three microstructure mor-

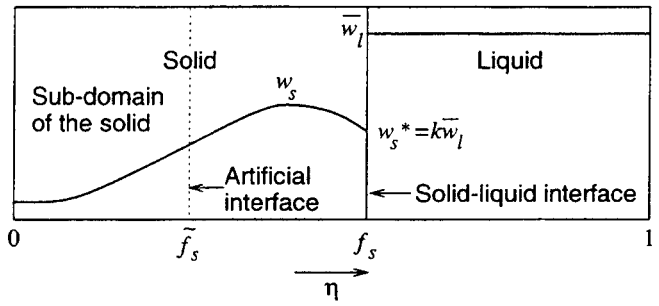

Fig. 2—Schematic solute profile in the solid and liquid phases of a platelike secondary dendrite arm, indicating the idea of the collocation method.

phologies (Eqs. [11], [14], and [15]) can be rewritten as a single equation as follows:

$$\frac{d\overline{w}_s}{dt} = \frac{k\overline{w}_l - \overline{w}_s}{f_s}\left[\frac{df_s}{dt} + \frac{D_s}{x_0^2}\frac{\zeta^2(\gamma+1)}{f_s^{(\frac{2}{\zeta}-1)}}\right] \quad [16]$$

where the particular choice of the adjustable parameter $\gamma = 2/\zeta$ reflects a parabolic solute profile, and ζ equal to 1, 2, and 3 represents the platelike, cylindrical, and spherical geometries, respectively.

E. *Collocation Method*

As will become apparent in the case studies, the internal variable approach and the power-law approximation are not capable of reproducing the changes of the solute profiles that occur during remelting. For that reason, a collocation method has been derived; it is equivalent of assuming a solute profile in the solid given by

$$w_s(\eta) = a + b\eta^2 + c\eta^3 \quad [17]$$

where again η is a dimensionless variable normalized with respect to one-half the secondary dendrite arm spacing, x_0 ($\eta \in [0, f_s(t)]$). Please note that the linear term has been omitted in Eq. [17] in order to satisfy the zero flux boundary condition at $\eta = 0$. The constants a, b, and c are determined at each time-step by a collocation method (as described in Reference 39). More specifically, they are calculated from the solute balances in the solid, the liquid, and a fixed subdomain within the dendrite arm (Figure 2). The solute balances in the solid and liquid phases can be written for a platelike morphology as

$$\frac{d}{dt}[f_s\overline{w}_s] = w_s^*\frac{df_s}{dt} + \frac{D_s}{x_0^2}\frac{\partial w_s^*}{\partial \eta} \quad [18]$$

and

$$\frac{d}{dt}[(1-f_s)\overline{w}_l] = \frac{dw}{dt} - w_s^*\frac{df_s}{dt} - \frac{D_s}{x_0^2}\frac{\partial w_s^*}{\partial \eta} \quad [19]$$

respectively, where the equilibrium condition at the interface, $w_s^* = k\overline{w}_l$, has been used again. The solute balance in a subdomain $\eta \in [0, \tilde{f}_s]$ gives

$$\frac{d}{dt}[\tilde{f}_s\tilde{\overline{w}}_s] = \frac{D_s}{x_0^2}\frac{\partial \tilde{w}_s}{\partial \eta} \quad [20]$$

where the tilde (~) denotes entities taken at the subdomain position. By using the relationships

$$\overline{w}_s = \frac{1}{f_s}\int_0^{f_s} w_s(\eta)\, dn = a + \frac{1}{3}bf_s^2 + \frac{1}{4}cf_s^3 \quad [21]$$

$$w_s^* = a + bf_s^2 + cf_s^3 \quad [22]$$

$$\frac{\partial w_s^*}{\partial \eta} = 2bf_s + 3cf_s^2 \quad [23]$$

$$\frac{\partial \tilde{w}_s}{\partial \eta} = 2b\tilde{f}_s + 3c\tilde{f}_s^2 \quad [24]$$

and assuming a certain value for $\tilde{f}_s$, *e.g.*, $\tilde{f}_s = f_s/2$, Eqs. [18] through [20] yield a set of three first-degree equations from which the parameters a, b, and c can be determined at each time-step.

F. *The One-Dimensional Diffusion Problem*

In order to compare and validate the various microsegregation approximations presented in the previous sections, the diffusion equation in one dimension

$$D_s\frac{\partial^2 w_s}{\partial x^2} = \frac{\partial w_s}{\partial t} \quad \text{for } x \in [0, x_s(t)] \quad [25]$$

where $x_s(t) = x_0 f_s(t)$ is the actual position of the solid-liquid interface, has been solved. A similar approach to the microsegregation problem has recently been discussed by Voller and Sundarraj.[24,25]

The boundary condition at $x = 0$ is that of a closed system (symmetry):

$$D_s\frac{\partial w_s}{\partial x} = 0 \quad \text{at } x = 0 \quad [26]$$

The boundary conditions that prevail at the moving solid-liquid interface are given by the local equilibrium condition on one hand and by a solute flux conservation on the other hand. The first condition is represented by Eqs. [3] and [5]. The flux condition at $x = x_s(t)$, which can be derived easily from the integral solute conservation equation, is given by

$$\frac{D_s}{x_0}\frac{\partial w_s}{\partial x} = \frac{dw}{dt} - (1-f_s)\frac{d\overline{w}_l}{dt} + (1-k)\overline{w}_l\frac{df_s}{dt} \quad \text{at } x = x_s(t) \quad [27]$$

The initial conditions correspond to $f_s = 0$ and $\overline{w}_l = w$ at $t = 0$.

III. SOLUTION ALGORITHMS

A. *Integration of the Evolution Equations*

Restarting the derivation from Eq. [6] and using Eq. [2], one has the general relationship

$$\frac{d}{dt}(f_s\overline{w}_s) = \frac{dw}{dt} - \frac{d}{dt}[(1-f_s)\overline{w}_l] = k\overline{w}_l\frac{df_s}{dt} + \Phi_{s/l}$$

or

$$\frac{d}{dt}[(1-f_s)\overline{w}_l] = \frac{dw}{dt} - k\overline{w}_l\frac{df_s}{dt} - \Phi_{s/l} \quad [28]$$

where $\Phi_{s/l}$ is the flux of solute at the solid-liquid interface

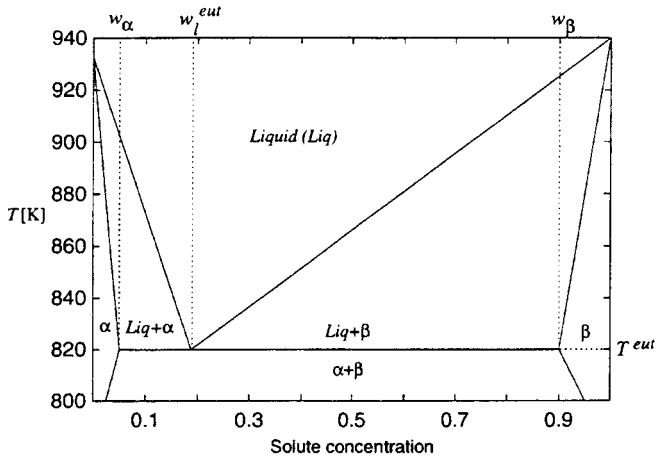

Fig. 3—Binary phase diagram.

Table I. Transformation Dynamics of the Volume Element

	t				
$t + \Delta t$	Liq	Liq + α	Liq + α + β	α + β	α
Liq	1	2	3	4	5
Liq + α	6	7	8	9	10
Liq + α + β	11	12	13	14	~~15~~
α + β	16	17	18	19	~~20~~
α	21	22	~~23~~	~~24~~	25

associated with back diffusion. Following what has been presented in Sections II–B through E, this term is equal to

$$\Phi_{s/l} = \frac{D_s}{x_0^2}\xi\frac{k\overline{w}_l - \overline{w}_s}{1 - (1 - k)f_s} = \frac{D_s}{x_0^2}\xi\frac{[1 - (1 - k)f_s]\overline{w}_l - w}{f_s[1 - (1 - k)f_s]} \quad [29]$$

for the internal variable approach

$$\Phi_{s/l} = \frac{D_s}{x_0^2}(1 + \gamma)\frac{k\overline{w}_l - \overline{w}_s}{f_s} = \frac{D_s}{x_0^2}(1 + \gamma)\frac{[1 - (1 - k)f_s]\overline{w}_l - w}{f_s^2} \quad [30]$$

for the power-law approximation, and

$$\Phi_{s/l} = \frac{D_s}{x_0^2}\frac{\partial w_s^*}{\partial \eta} \quad [31]$$

for the collocation method and the one-dimensional diffusion equation, respectively. For the first two approaches, the term $\overline{w}_s$ which appears in the flux (Eqs. [29] and [30]) has been replaced using again Eq. [2] so as to keep only $\overline{w}_l$ and w. For the other two methods, the solute profiles are calculated.

The average solute content of the small-volume element, $w(t)$, is assumed to be a known function of time. For a closed system, $w(t)$ is constant and equal to the nominal concentration of the alloy, w_0, whereas for an open system, $w(t)$ is deduced from the macroscopic continuity equations (Figure 1). Accordingly, Eq. [28] allows to calculate $\overline{w}_l$ as a function of f_s. Using a time-marching scheme with a time-step Δt, one obtains

$$\frac{(1 - f_s^{t+\Delta t})\overline{w}_l^{t+\Delta t}}{\Delta t} - \frac{(1 - f_s)\overline{w}_l}{\Delta t} = \frac{w^{t+\Delta t} - w}{\Delta t} - k\overline{w}_l^{t+\Delta t}\left(\frac{f_s^{t+\Delta t} - f_s}{\Delta t}\right) - \Phi_{s/l}^{t+\Delta t} \quad [32]$$

by which $\overline{w}_l^{t+\Delta t}$ can be determined for any value of the solid fraction, including $f_s^{t+\Delta t} = 1$. (The quantities without the superscript $(t + \Delta t)$ in Eq. [32] stand for values at time t).

B. *Solidification Dynamics and Eutectic Reaction*

Considering the phase diagram of Figure 3, several situations can be encountered for a small volume element during one time-step. At the beginning of a time-step, the volume element can be in five different "states": fully liquid (Liq), mushy with the presence of the primary phase only (Liq + α), mushy with some primary phase and some eutectic (Liq + α + β), fully solid with some interdendritic eutectic (α + β), and fully solid without eutectic (α). These various states are also labeled in the phase diagram of Figure 3. Because the entire solidification is assumed to start with a hypoeutectic alloy of uniform concentration, macroscopic transport of solute cannot bring a point of the domain to a hypereutectic state (*e.g.*, presence of liquid and β without α). On the other hand, it must be emphasized that the eutectic reaction (Liq + α + β) in a binary alloy occurs at fixed temperature and concentration according to Gibbs rules.

As indicated by Table I, the final state of the volume element at time $t + \Delta t$ is also characterized by (Liq), (Liq + α), (Liq + α + β), (α + β), or (α). In total, there are 25 possibilities describing the solidification dynamics of the system, but four of them are discarded: formation of eutectics upon cooling from a supersaturated α solution when crossing the solvus α line (case 20), dissolution of eutectics upon cooling in the solid state (case 24), remelting of α with spontaneous formation of β (case 15), and end of solidification with disappearance of β (case 23). Accordingly, 21 situations can occur. For example, cases 1, 19, and 25 correspond to the simple cooling (or heating) of the liquid or solid. Cases 16 and 21 would be those of a complete solidification occurring within one time step, whereas the symmetric situations 4 and 5 are those of full remelting, *etc.*

It might look straightforward to determine what will happen to a volume element once its new specific enthalpy, $h^{t+\Delta t}$, and solute concentration, $w^{t+\Delta t}$, are known. However, this is not the case due to the possible formation (or dissolution) of eutectics. The procedure is as follows. First, the enthalpy, $h_{liq}^{t+\Delta t}$, of a volume element that is liquid at the liquidus temperature defined by $w^{t+\Delta t}$ is calculated

$$h_{liq}^{t+\Delta t} = c_p(T_m + mw^{t+\Delta t}) + L \quad [33]$$

Second, the temperature of the last solid to form, T_α, is calculated by substituting $f_s^{t+\Delta t} = 1$ into Eq. [32] under the assumption of no eutectic formation and inserting the obtained value of $\overline{w}_l$ into Eq. [3]. If T_α is found to be smaller than the eutectic temperature, T^{eut}, then T_α is set equal to T^{eut}. The associated fraction of solid, f_s^{eut}, that could form before the beginning of the eutectic precipitation is also

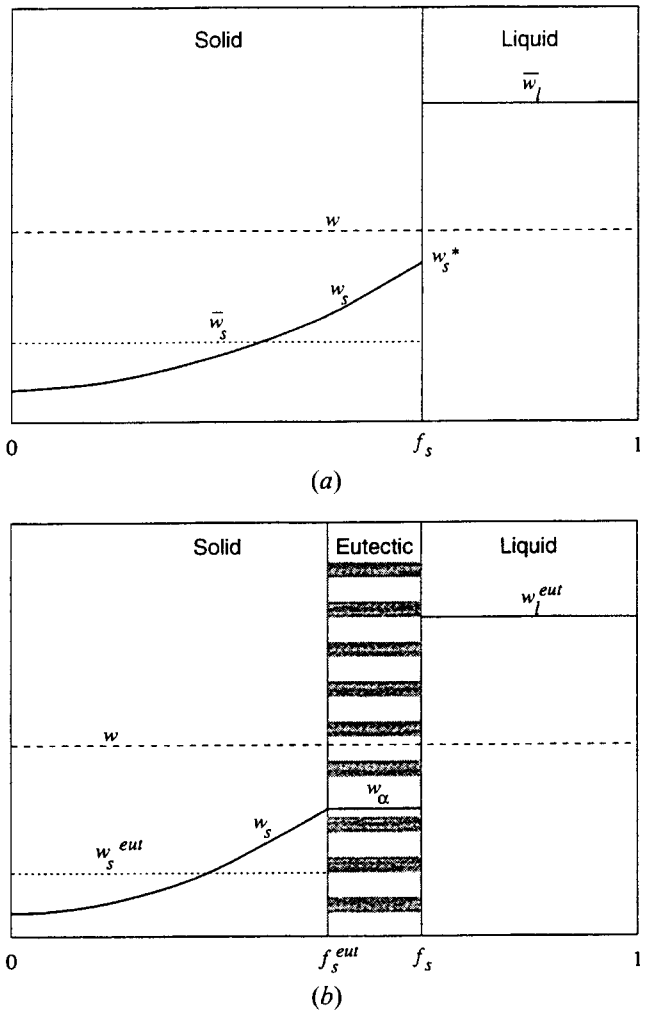

Fig. 4—Schematic concentration profiles when (*a*) no eutectic and (*b*) some eutectic have formed.

calculated by solving the microsegregation problem up to the value $\bar{w}_l(T^{eut}) = w_l^{eut}$ where w_l^{eut} is the eutectic concentration (Figure 3). The enthalpy corresponding to the beginning of the eutectic precipitation, h_α^{eut}, is defined as

$$h_\alpha^{eut} = c_p T^{eut} + L(1 - f_s^{eut}) \quad [34]$$

The various cases that can occur then are as follows:

	$h^{t+\Delta t} > h_{liq}^{t+\Delta t}$	the cell is fully liquid (Liq)
$T_a > T^{eut}$	and $h^{t+\Delta t} > h_a = c_p T_a$	the cell is mushy without eutectic (Liq + α)
$T_a > T^{eut}$	and $h^{t+\Delta t} \le h_a = c_p T_a$	the cell is fully solid without eutectic (α)
$T_a = T^{eut}$	and $h^{t+\Delta t} > h_\alpha^{eut}$	the cell is mushy without eutectic (Liq + α)
$T_a = T^{eut}$	and $h_\alpha^{eut} > h^{t+\Delta t} > c_p T^{eut}$	the cell is mushy with eutectic (Liq + α + β)
$T_a = T^{eut}$	and $h^{t+\Delta t} \le c_p T^{eut}$	the cell is fully solid with eutectic (α + β)

In the absence of a eutectic precipitation (Figure 4(a)), the temperature is considered to be a nonlinear function of the volume fraction of solid through Eqs. [1], [3], and [32]. The searched value of $f_s^{t+\Delta t}$ is then given by the zero of the function

$$) = h^{t+\Delta t} - c_p T(\bar{f}_s) - L(1 - \bar{f}_s) \quad [35]$$

where $T(\bar{f}_s) = T_m + m\bar{w}_l(\bar{f}_s)$ (Eq. [3]) and $\bar{w}_l(\bar{f}_s)$ is the solution of the microsegregation problem (Eq. [32]) when $f_s^{t+\Delta t}$ is set equal to the arbitrary value $\bar{f}_s$. The zero of the function $g(\bar{f}_s$ is determined using the algorithm of Brent (as described in Reference 40).

When some eutectic has formed (Figure 4(b)), the problem is made difficult for two reasons. First, back diffusion in the primary phase can partially dissolve some of the eutectics that has formed previously, and second, a variation of the liquid concentration can bring the open system out of the purely eutectic reaction (*e.g.*, the system will again become hypoeutectic if w decreases). These two problems have been simplified as follows. First, the mass fraction of the primary phase at the beginning of the eutectic reaction, f_s^{eut}, is assumed to be "frozen," and the solute profile in the primary phase is fixed. Second, small deviations from the eutectic composition are assumed to change slightly the fractions of phases f_α and f_β that form during the eutectic precipitation but without affecting the temperature. Thus, these mass fractions are calculated from the two equations

$$w = (1 - f_s)w_l^{eut} + f_s^{eut} w_s^{eut} + f_\alpha w_\alpha + f_\beta w_\beta \quad [36]$$

$$f_s = f_s^{eut} + f_\alpha + f_\beta \quad [37]$$

where w_α, w_β and w_l^{eut}, and w_s^{eut} are the solute concentrations in the two eutectic phases, the eutectic liquid concentration, and the average solid concentration in the primary phase just before eutectic precipitation, respectively (Figure 3).

The initial value for $\bar{w}_l$ at the beginning of solidification is set equal to the current value of w. If remelting occurs after the solidification has been completed, the initial value for $\bar{w}_l$ is taken to be the eutectic value, w_l^{eut}, if solidification was completed at the eutectic temperature. If the solidification was completed above the eutectic temperature, the estimated solute concentration at the calculated solidus temperature is applied as the initial value. The possibility of remelting is detected by the condition $h^{t+\Delta t} > h_\alpha = c_p T_\alpha$ (*i.e.*, the new enthalpy is greater than the enthalpy of the last solid to have formed). The solute profile in the primary phase that was previously frozen can then evolve again, and the solidus temperature, T_α^*, has to be recalculated taking into account the diffusion in the solid. Remelting will effectively occur if $h^{t+\Delta t} > h_\alpha^* = c_p T_\alpha^*$.

C. *Solution of the One-Dimensional Diffusion Problem*

A finite-difference method has been used for solving the microsegregation problem defined in Section II–E, and similar to Voller and Sundarraj,[24,25] a Landau transformation[41,42] which maps the solid domain onto the [0,1] interval has been made. With reference to the Appendix for the details, the equation that has to be solved in the interval [0,1] is

$$\frac{D_s}{x_0^2 f_s^2}\frac{\partial^2 w_s}{\partial \varepsilon^2} - \frac{\partial w_s}{\partial t} + \frac{\varepsilon}{f_s}\frac{df_s}{dt}\frac{\partial w_s}{\partial \varepsilon} = 0 \quad [38]$$

where ε is the nondimensional parameter ($\varepsilon \in [0,1]$). For all the internal nodes (Figure 5), this equation is solved using finite differences, a fully implicit scheme, and upwinding (please note, however, that the advection term in Eq. [38] is small compared to diffusion).

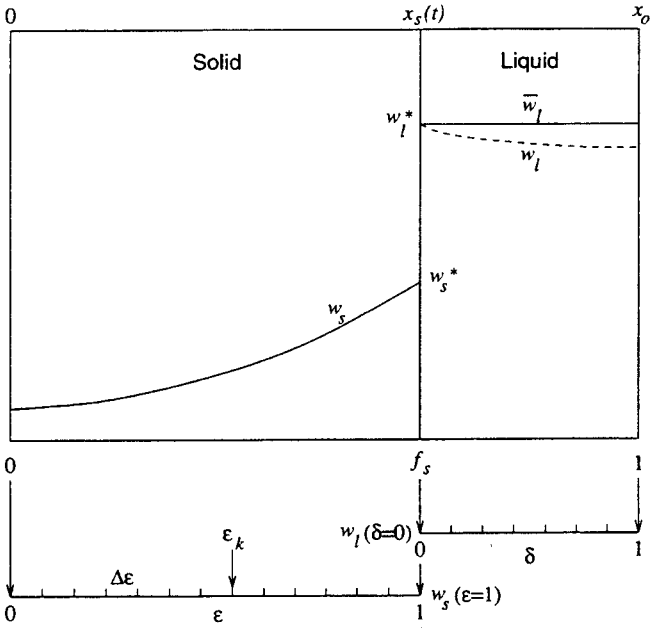

Fig. 5—Concentration profiles in solid and liquid (Section III-C) and associated Landau transformations. Continuous line: complete solute redistribution in the liquid; dashed line: finite solute redistribution in the liquid.

Table II. Material Parameters for the Aluminum Model Alloy

Heat capacity	c_p	1080 J K g^{-1} K^{-1}
Latent heat of fusion	L	388×10^3 J K g^{-1}
Solute diffusivity in the solid	D_s	9×10^{-12} m^2 s^{-1}
Half secondary dendrite arm spacing	x_0	30×10^{-6} m
Melting temperature	T_m	933 K
Liquidus slope	m	−600 K
Partition coefficient	k	0.25 —
Eutectic temperature	T^{eut}	820 K
Eutectic liquid concentration	w_l^{eut}	0.188 —
Solute concentrations in the eutectic phases	w_α and w_β	0.047 and 0.9 —

The boundary condition at $\varepsilon = 0$ is that of a closed system

$$\frac{\partial w_s}{\partial \varepsilon} = 0 \quad \text{for } \varepsilon = 0 \qquad [39]$$

Assuming that solute is completely mixed within the liquid phase, the boundary condition at the solid-liquid interface position is given by

$$\frac{D_s}{x_0^2 f_s}\frac{\partial w_s}{\partial \varepsilon} = \frac{dw}{dt} - (1 - f_s)\frac{\bar{w}_l^{t+\Delta t} - \bar{w}_l}{\Delta t} + (1 - k)\frac{df_s}{dt}\bar{w}_l^{t+\Delta t} \quad \text{for } \varepsilon = 1 \qquad [40]$$

Since $w_s = k\bar{w}_l$ when $\varepsilon = 1$, Eq. [40] is a mixed-boundary condition provided that the variations of w and of f_s are known. The first entity comes from the macroscopic solute conservation equation. The value of df_s/dt is guessed by imposing a new value to $f_s^{t+\Delta t}$. The microsegregation equation is then solved using this mixed-boundary condition, and the process is iterated until the temperature deduced from the new value of $\bar{w}_l^{t+\Delta t}$ matches that obtained from the heat balance with the corresponding value of df_s/dt. The same algorithm as the one used for solving Eq. [35] is employed. Overall variations of the average solute concentration, w, are instantaneously distributed within the liquid phase.

In order to assess the influence of the complete mixing assumption made for the liquid phase, a calculation of solute diffusion in the liquid (Figure 5) has also been performed. Two Landau transformations have been used in this case, and the velocity of the solid-liquid interface is given by the solute flux condition at the interface

$$\frac{D_s}{x_0^2 f_s}\frac{\partial w_s}{\partial \varepsilon} - \frac{D_l}{x_0^2(1 - f_s)}\frac{\partial w_l}{\partial \delta} = (1 - k)\frac{df_s}{dt}w_l \quad \text{for } \varepsilon = 1 \text{ (and } \delta = 0) \qquad [41]$$

Here, w_l is the concentration in the liquid phase, D_l is the solute diffusion coefficient in the liquid, and the parameter δ is used for the Landau transformation in the liquid phase. The resolution procedure is similar in this case, Eq. [41] being again a mixed-boundary condition for the solid and liquid phases when the problems in these two phases are coupled. The supplementary condition that must be applied in the liquid phase at $\delta = 1$ is given in this case by

$$\frac{D_l}{x_0^2(1 - f_s)}\frac{\partial w_l}{\partial \delta} = \frac{dw}{dt} \quad \text{for } \delta = 1 \qquad [42]$$

Please note that this condition resumes to that of a closed system when w is constant in the volume element. Overall variations of the average solute concentration, w, are specified as an input flux.

IV. CASE STUDIES

A binary aluminum model alloy with the simplified phase diagram shown in Figure 3 is considered. Other simplifications are the assumptions of constant latent heat of fusion, L, constant and equal density and heat capacity, c_p, of the liquid and solid phases, and constant solute diffusivity in the solid, D_s. The phase diagram characteristics (partition coefficient, k, and liquidus slope, m) are also taken as constant. The values of the material constants including those defined in Figure 3 are given in Table II. Typical for commonly used aluminum alloys, they are such that the difference between the Scheil and lever rule solidification paths is fairly significant. Furthermore, the ratio $D_s/x_0^2 = 0.01$ s^{-1} is such that a solidification path between the Scheil and lever rule limits is obtained for the solidification times encountered in most conventional casting processes.

A. *Solidification Case, Closed System*

A closed one-dimensional volume element whose characteristics are given in Table II is first solidified under the condition of a linearly decreasing enthalpy. The three sets of curves shown in Figure 6(a) correspond to an enthalpy slope of −30, −3, and -0.3×10^3 J Kg^{-1} s^{-1}, thus leading to solidification times of about 15, 150, and 1500 seconds, respectively. For each solidification condition, the temper-

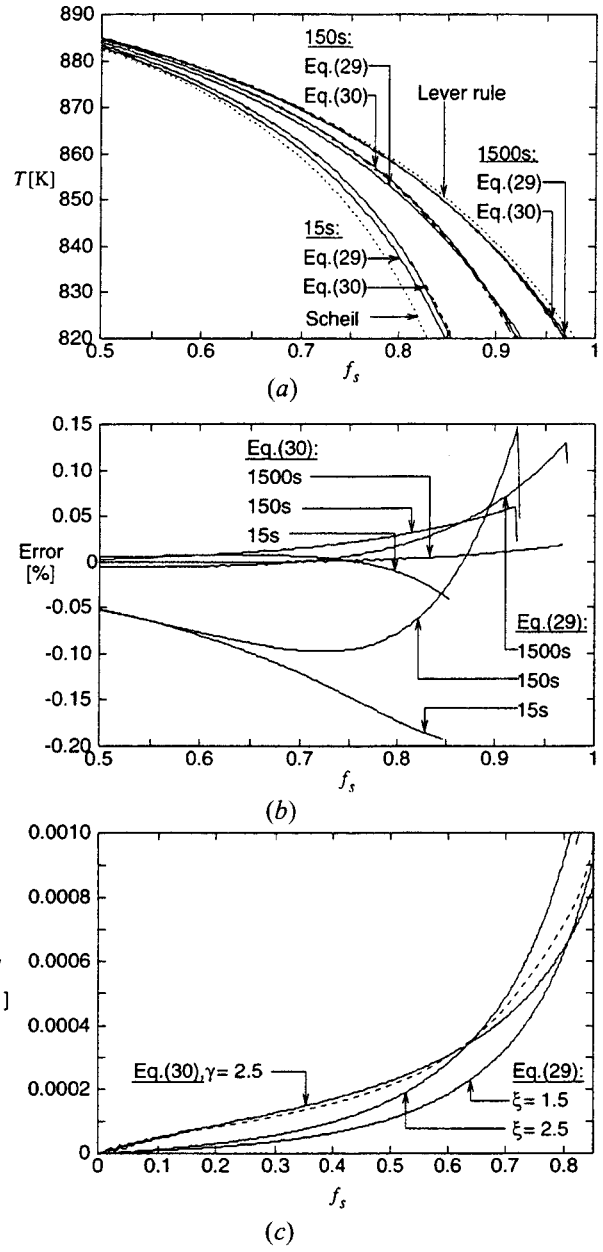

Fig. 6—(*a*) Temperature *vs* solid fraction resulting from calculations in which there is a steadily decreasing enthalpy corresponding to solidification times of about 15, 150, and 1500 s. The total solute concentration is 0.05 and constant. Exact results (dashed curves) are shown along with results obtained with the internal variable models: Eq. [29] with $\xi = 1.5$ and Eq. [30] with $\gamma = 2.5$. The Scheil and lever rule limits (dotted curves) are also shown. (*b*) Relative error in the temperature *vs* solid fraction for the internal variable modeling results of (a). (*c*) Interfacial solute flux *vs* solid fraction for the situation described in (a) with the shortest solidification time (about 15 s). The exact result (dashed curve) is shown along with the results obtained by using Eq. [29] with $\xi = 1.5$ and $\xi = 2.5$ and Equation [30] with $\gamma = 2.5$.

ature has been plotted as a function of the fraction of solid according to the two approximate models: the curves labeled "Eq. [29]" and "Eq. [30]" correspond to the solute flux approximations of Eqs. [29] and [30], respectively. The internal variable model (Eq. [29]) has been used with $\xi = 1.5$, whereas the power-law approximation (Eq. [30]) corresponds to $\gamma = 2.5$. For each solidification condition, these two curves are compared with the "exact" solution given by the dashed curve, *i.e.*, solute flux given by Eq. [31]. Although this solution is based on a finite-difference method and a coordinate transformation, it will be called "exact solution" subsequently. The two extreme cases of Scheil and lever rule approximations are also displayed in this figure with dotted lines. In all the cases shown in Figure 6(a), the average solute concentration, w, is constant and equal to 0.05 (closed system).

Similarly to what has been shown previously in References 26 and 28, the results obtained with the approximate models give fairly accurate results for all three solidification times. As can be seen in Figure 6(a), the agreement is better for the model based upon the power-law approximation of the solute profile (Eq. [30]). This is emphasized in Figure 6(b), in which the relative error* in temperature is plotted as a function of the fraction of solid.

* The relative error is defined as the difference between the temperature obtained with the approximate model (Eqs. [29] or [30]) and that given by the exact solution (solute flux given by Eq. [31]), this difference being normalized with the temperature.

A deeper insight into the models can be gained through a study of the variation of the approximated term in the equations, namely, the interfacial solute flux in the solid, $\Phi_{s/l}$. This calculated flux is plotted in Figure 6(c) as a function of the fraction of solid for the shortest solidification time (about 15 seconds), *i.e.*, for the case in which the largest discrepancy between the approximate and exact solutions is observed (Figures 6(a) and (b)). The flux calculated with the finite-difference technique (dashed curve) can be compared with the results obtained with the two approximate models for different values of the adjustable parameters. As can be seen, the model represented by Eq. [30] is fairly accurate with $\gamma = 2.5$, whereas the model represented by Eq. [29] with $\xi = 1.5$ gives a solute flux which is too low over the entire solidification range. An increase of the value of ξ to 2.5 leads to a flux which is still too low at the beginning of solidification but which then becomes too large near the end. Hence, it can be concluded for a closed solidifying system that the power-law model (solute flux given by Eq. [30]) gives a better approximation of the microsegregation problem than Eq. [29] originally proposed in Reference 28. Therefore, only the power-law solute profile approximation (Eq. [30]) will be considered in the remainder of the article.

Concerning the determination of the adjustable parameters, it should be pointed out that the particular value $\gamma = 2.5$ used in Figure 6 has been chosen because it is close to the minimum of the relative absolute error averaged over the entire solidification path for any of the solidification times 15, 150, and 1500 seconds. It turns out that the corresponding relative error in $\overline{w}_l$ is only 0.1 pct for this particular choice of γ, whereas that in $\overline{w}_s$ can be up to about 0.5 pct. Another choice of γ, within the accuracy of the curves in Figure 6, would not have given any better agreement between approximate and exact solutions (neither would another choice of the adjustable parameter ξ).

B. *Solidification/Remelting Case, Closed System*

When a closed system is continuously solidifying, the solute profile in the solid has a curvature of constant sign over the entire solidification path (*e.g.*, the slope of the profile is a monotonically increasing function of f_s if $k <$

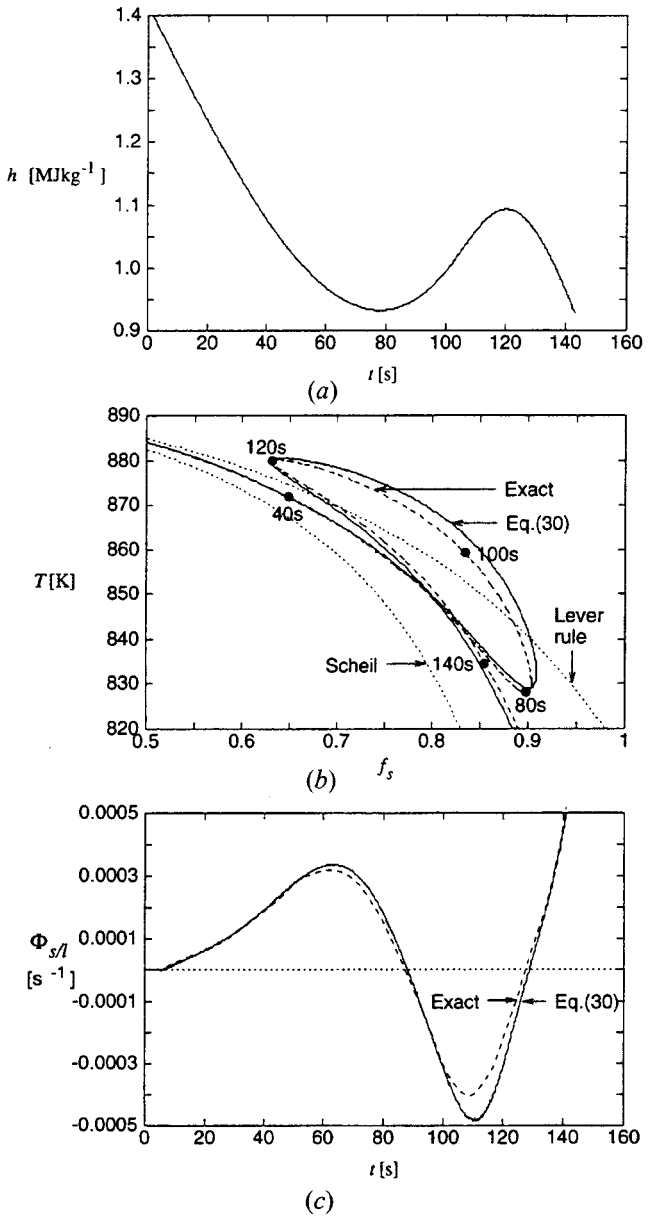

Fig. 7—(*a*) Imposed enthalpy *vs* time, (*b*) corresponding solidification path, and (*c*) interfacial solute flux. Average concentration: $w = 0.05$ = constant. The continuous curves in (b) and (c) have been calculated with the power-law approximation (Eq. [30] with $\gamma = 2.5$), and the exact results are shown as dashed curves. In (b), the Scheil and lever rule limits are shown as dotted curves, and the various points and times labeled on the exact curve correspond to the times in (a) and (c). (These times are not set up for the two extreme cases of Scheil and lever rule because the solidification and remelting parts of these two paths are superimposed under the assumption of a closed system.)

1). This explains why a power-law approximation of this profile can give a fairly high accuracy when the enthalpy is steadily decreasing (*cf.* Section IV–A). However, this does not necessarily imply that the model provides an accurate description of remelting situations. In order to assess the accuracy of the model based upon the power-law approximation in such situations, the enthalpy variation displayed in Figure 7(a) is considered for a closed system (constant concentration of 0.05). During the first 80 seconds, the alloy solidifies. It then remelts during the next 40 seconds before being resolidified. With the selected material constants and the time allowed for solid-state diffusion,

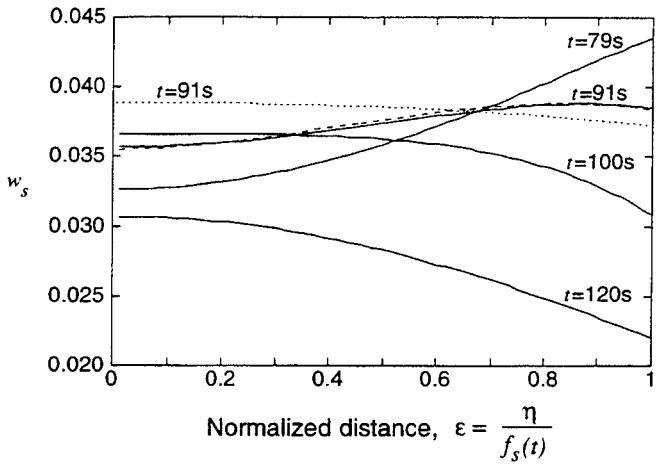

Fig. 8—Calculated solute profiles in a platelike secondary dendrite arm at different times corresponding to Fig. 7. The dotted and dashed curves for $t = 91$ s correspond to the power-law (Eq. [30] with $\gamma = 2.5$) and cubic approximations of the solute profile, respectively. The other profiles (continuous curves) have been obtained with the exact solution.

the solidification path during the first 40 seconds should be typically in-between those predicted by the Scheil and lever rule limits.

The solidification path corresponding to the variation of enthalpy shown in Figure 7(a) is displayed in Figure 7(b). In addition to the Scheil and lever rule limits, two curves have been plotted: the continuous curve corresponds to the solidification path calculated with the power-law approximation (Eq. [30] with $\gamma = 2.5$), whereas the dashed curve is the exact solution (Eq. [31]). The various points and times labeled on the exact curve correspond to the times in Figure 7(a). As can be seen in Figure 7(b), the approximate and exact solutions are in fairly close agreement: they both predict a loop during the remelting period. This agreement is emphasized in Figure 7(c), in which the interfacial solute flux in the solid is plotted *vs* time for the two models (Eqs. [30] and [31]). However, it can be seen in this figure that the approximate model is not as accurate when there is a change of sign in the enthalpy slope, *i.e.*, when the alloy starts to remelt near $t = 80$ and when it starts to resolidify near $t = 120$ s.

The discrepancy of the calculated solute fluxes during the remelting period is also reflected in the solidification paths of Figure 7(b). As already noticed in Reference 28, the temperature during this period becomes higher than the value predicted by the lever rule. It is in fact higher for the approximate model (Eq. [30]) than for the exact solution (Eq. [31]). As shown in Figure 7(c), this corresponds to the period of a negative solute flux at the interface. During this time, the average solute concentration in the solid, $\overline{w}_s$, becomes larger than the value at the interface, w_s^*. As illustrated in Figure 8, this phenomenon is closely linked with a reversal in the shape of the solute profile in the solid. In this figure, the solute profiles, $w_s(\varepsilon)$, calculated with the exact model are plotted as a function of the normalized variable, $\varepsilon = \eta/f_s(t)$, for various times (*i.e.*, $\varepsilon \in [0,1]$). At time $t = 79$ s, *i.e.*, before the start of remelting, the shape of the solute profile is concave (second derivative of $w_s(\varepsilon)$ is positive). At time $t = 91$ s, remelting has already taken place and the solute profile becomes convex near the interface. As a matter of fact, the maximum of $w_s(\varepsilon)$ predicted

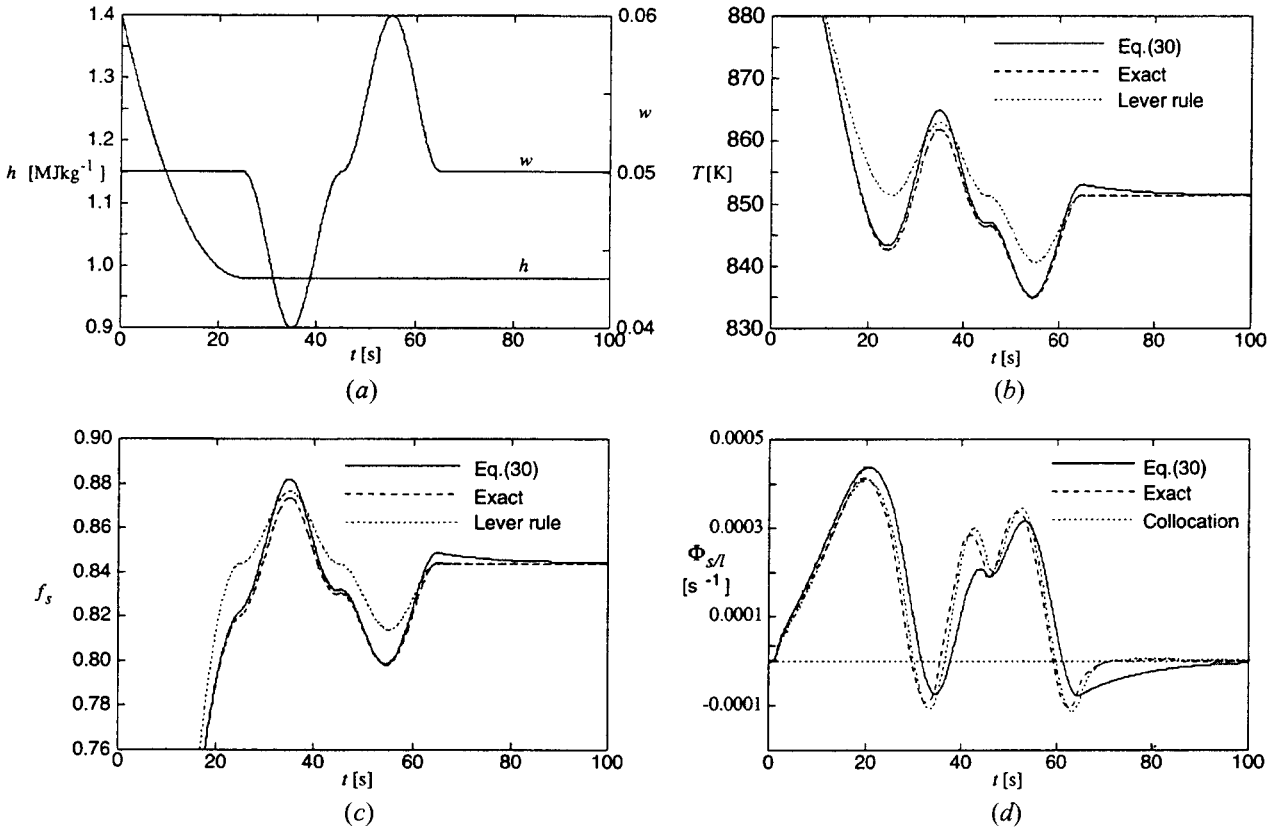

Fig. 9—(*a*) Enthalpy and average solute concentration variations, (*b*) corresponding temperature, (*c*) fraction of solid, and (*d*) interfacial solute flux. The continuous and dashed curves correspond to the power-law approximation (Eq. [30] with $\gamma = 2.5$) and the exact solution, respectively. The dotted lines in (b) and (c) show the lever rule limit. In (d), the dotted line has been obtained with the collocation method.

from the exact solution of the diffusion problem does no longer occur at the interface position ($\varepsilon = 1$ or $\eta = f_s(t)$). At the same time, the concentration decreases at the solid-liquid interface while it still increases at the center of the dendrite arm ($\varepsilon = 0$). The maximum of the solute concentration is gradually displaced towards $\varepsilon = 0$ as can be seen from the profile drawn at $t = 120$ s (*i.e.*, just before resolidification takes place).

This complex behavior of the solute profile at the onset of remelting (or more generally at any change of the interface movement direction) cannot be approximated by the simple power-law approximation represented by Eq. [8], and it explains why the solute profile at the onset of remelting is not so well approximated by the power-law model (dotted curve) at $t = 91$ s.* These observations were

*The two curves obtained at $t = 91$ s with the power-law and exact models seem to have different integrals and thus to characterize various solute contents. However, this does not mean that the models do not conserve solute since at that time, the associated fraction of solid (and hence position of the solid-liquid interface) and temperature (or value of w_l) are different.

the incentive to develop the third approximate model based upon a cubic polynomial approximation of the solute profile (*cf.* Section II–D), which turned out to give results that are very close to the exact solution. As an example, the dashed solute profile shown in Figure 8 for $t = 91$ s has been calculated with this method under the conditions specified in this Section: it is almost identical to the exact profile. The solidification path predicted with the collocation method for the remelting situation discussed previously has not been drawn in Figure 7(b) because it would have been almost indistinguishable from the exact solution.

Compared to the transformed coordinate finite difference solution of Fick's second law, the collocation method is less CPU time consuming while offering a similar precision. Compared to the internal variable approach and the power-law approximation, the collocation method is more accurate, especially when reversal in the solidification direction occurs. However, the associated computation cost is slightly higher since more equations have to be solved numerically. More specifically, the CPU time on a HP* 735 Workstation for the case described in Section IV–B is 0.23, 0.25, and 0.38 seconds for the power-law approximation, the collocation method, and the solution of the exact diffusion problem with 50 mesh points, respectively.**

*HP is a trademark of the Hewlett-Packard Company, Colorado Springs, CO.

**Recent calculations with a finite-difference solution and a nonuniform mesh refined near the solid-liquid interface have shown that accurate solutions can also be reached with very few nodal points (typically five or six nodes), thus reducing also the computation time.

C. *Solidification/Remelting, Open System*

Macrosegregation is associated with variations in the average solute concentrations at the scale of the process mainly induced by convection: they can range up to ± 100 pct of the nominal alloy element concentration.[43,44,45] Un-

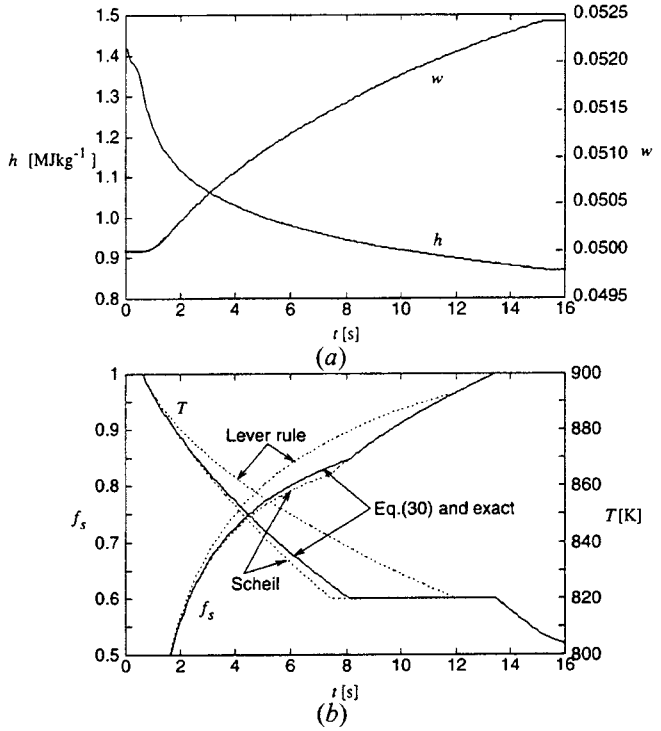

Fig. 10—(*a*) Enthalpy and average solute concentration variations pertaining to the case of inverse segregation and (*b*) corresponding evolutions of the temperature and fraction of solid. The continuous curves correspond to the power-law approximation (Eq. [30] with $\gamma = 2.5$) or the exact solution (*i.e.*, the power-law results are very close to the exact results). The lever rule and Scheil limits are shown as dotted curves.

der such conditions, the small-volume element associated with the dendrite arm spacing is no longer a closed system. In order to test the various microsegregation models for such an open system, variations of the average solute concentration, w, have been imposed as indicated in Figure 9(a). As can be seen in this figure, the average solute concentration, w, is kept constant and equal to 0.05 while the enthalpy, h, decreases during the first 25 seconds. The enthalpy is then kept constant, and the average concentration is first lowered by 20 pct between 25 and 45 seconds (negative segregation) and then increased by 20 pct between 45 and 65 seconds (positive segregation). Both the enthalpy and solute concentration are kept constant at times longer than 65 seconds.

The cooling curve, $T(t)$, and evolution of the fraction of solid, $f_s(t)$, associated with the enthalpy and solute curves shown in Figure 9(a) are displayed in Figures 9(b) and (c), respectively. (Please note that the variations of $f_s(t)$ when h is constant are closely associated with the variations of $T(t)$ since the heat balance has to be satisfied (Eq. [1])). The continuous curves are those calculated with the power-law approximation (Eq. [30]), the dashed ones are the results of the exact solution (Eq. [31]), and the dotted lines correspond to the lever rule approximation.* As can be seen in Figure 9(c), the system can still solidify or remelt under adiabatic conditions (h = constant) due to variations of the overall solute content. Remelting (solidification) could even occur for a decreasing (increasing) enthalpy if the increase (decrease) of the average concentration is sufficiently large. These are precisely the conditions under which freckles can form in the mushy zone.[46]

Figure 9 reveals that fairly accurate results can be obtained using the power-law approximation of the solute profile (Eq. [30]) even under the conditions of an open system. The normalized interfacial solute fluxes displayed in Figure 9(d) indeed show that this model can reasonably accommodate variations of the average solute concentration. As in Section IV–B, however, there are periods of rather poor agreement between the approximate and exact solutions, especially when the variation of the interfacial solute flux is not monotonic. Again, the approximate solution obtained with the collocation method does not present this drawback and is very close to the exact solution.

The case study corresponding to Figure 9 has been carried out mainly to assess the limitations of the approximate models for an open system. It is therefore of interest to study a case in which the inputs, $h(t)$ and $w(t)$, are taken from a "realistic" macrosegregation computation. Such a study can provide interesting results even without the full micro-macrosegregation coupling. The input shown in Figure 10(a) has been obtained from Reference 12: it corresponds to the inverse segregation calculated near a cast surface during directional solidification and to the same material data as in Table II.* The cooling curve, $T(t)$, and fraction of solid, $f_s(t)$, corresponding to the variations of enthalpy, $h(t)$, and solute concentration, $w(t)$, of Figure 10(a) are shown in Figure 10(b). The continuous curves correspond to both the power-law approximation (Eq. [30] with $\gamma = 2.5$) and the exact solution (Eq. [31]), since the results almost coincide. The results obtained with Scheil and the lever rule approximations are also shown.** Since the solidification time is rather short near the surface of the casting (about 14 seconds), the computed results are much closer to the Scheil limit than the lever rule. However, it should be kept in mind that the dendrite arm spacing, which was kept constant for all the calculations (60 μm), is expected to be smaller when the cooling rate increases, thus reducing the Fourier number for solute diffusion in the solid.

Although the present calculations of the solidification path are not yet fully coupled with a macrosegregation computation (*i.e.*, the macrosegregation was first estimated using the lever rule, and the variations of enthalpy and solute content were then used as input to the microsegregation model), the microsegregation results shown in Figure 10 for a realistic value of D_s (or more precisely of the Fourier number) indicate a need for applying a model more realistic than the lever rule. Furthermore, they clearly show that the power-law approximation model is a good alternative to the numerical solution of the microsegregation problem, at least when there is no remelting.

*The results corresponding to the Scheil approximation ($D_s = 0$) cannot be displayed because, as mentioned in Ref. 33 and 34 this approximation introduces a singular point at the interface under the condition of remelting of an open system.

*In Ref. 12, the macrosegregation calculation was carried out according to the lever rule approximation, and the eutectic reaction at the end of solidification was not taken into account. The thermal boundary condition at the cast-mold interface was given by a constant heat transfer coefficient of 2500 W m^{-2} K^{-1}.

**The Scheil result can be computed without any problem in this case since there is no period of remelting.

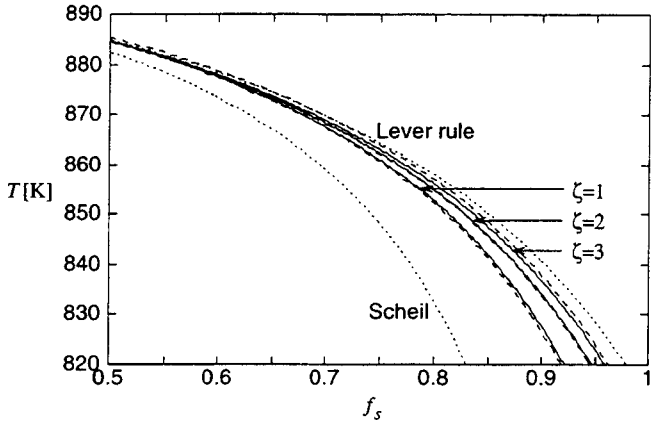

Fig. 11—Effect of the microstructure morphology on the calculated solidification path. The enthalpy is steadily decreasing and gives a solidification time of about 150 s (Fig. 6(a)). The total solute concentration is 0.05 and constant. The results are obtained with the internal variable model using Eq. [16] with $(\gamma\zeta) = 2.5$ and the "morphology factor" ζ equal to 1 (platelike), 2 (cylindrical), and 3 (spherical). Exact results (dashed curves) along with the Scheil and lever rule limits (dotted curves) are also shown.

V. DISCUSSION

Solidification shrinkage and pore formation, which in the present investigation has not been taken into account, can have an effect upon the formation of macrosegregation.[47–50] Studying their effect on the local solidification path requires a fully coupled micro-macrosegregation calculation. The previously discussed microsegregation approaches could easily include shrinkage by interpreting f_s as the *volume* (rather than *mass*) fraction of solid and by introducing the (different) solid and liquid densities in the equations.

Also, dendrite coarsening is neglected. However, the effect of this phenomenon upon the local solidification path of a closed system has been found to be rather limited.[23,51]

The thermophysical and diffusivity parameters, which in the present study have been taken as constants, could easily be made temperature and/or solute-concentration dependent. The formalism for solving the exact diffusion problem as well as the different approximative methods are all quite general and would allow such an extension.

The presented methodologies can also be extended to apply for multicomponent alloys provided that the phase-diagram characteristics are known. The concentration $\overline{w}_l$ appearing in Eqs. 28 through 31, has purposely not been replaced by the temperature, which could have been done for a binary alloy. For a multicomponent alloy, diffusion of the various solute elements in the primary phase requires one evolution equation per element,[28] whereas the liquidus surface is a unique function of all the concentrations, *i.e.*, Eq. [3] must be interchanged with

$$T = T_m + \int_0^{\overline{w}_l^i} \sum_i^n m^i(\overline{w}_l^1, \overline{w}_l^2, \ldots, \overline{w}_l^n) \cdot d\overline{w}_l^i \qquad [43]$$

The precipitation of secondary phases in a multicomponent alloy is certainly more difficult to handle (binary eutectic, ternary eutectic, *etc.*).

In order to assess the effect of morphology (*cf.* Section II–C), the temperature *vs* fraction of solid for the intermediate solidification conditions of Figure 6(a) has been calculated for the three values of the "morphology factor" ζ. The results are shown in Figure 11, in which the continuous curves have been calculated with Eq. [16] with $(\gamma\zeta) = 2.5$. The results corresponding to ζ equal to 1, 2, and 3 are compared with the corresponding finite-difference solutions of the diffusion equation written for the corresponding geometries.* As could be expected, diffusion from the solid-liquid interface is favored when going from a platelike to a spherical geometry (*i.e.*, when ζ increases from 1 to 3). Accordingly, the solidification path moves closer to the lever rule limit as ζ increases. Furthermore, the power-law approximation gives results which are close to the numerical solution of the microsegregation problem, regardless of the geometry being chosen.

*The Landau transformation method is similar to that described in Section III–C, the only difference being the form of the Laplacian operator.

In most aluminum alloys, the liquid diffusivity, D_l, is typically three orders of magnitude larger than the solid diffusivity, D_s. This is why in microsegregation models, the liquid is assumed to have locally a uniform concentration (*i.e.*, complete mixing). However, this assumption is usually made for a closed, solidifying system. In order to assess the effect of liquid diffusion in open systems and/or in systems with remelting, the microsegregation problem encompassing diffusion also in the liquid phase has been solved numerically (Section III–C). The value $D_l = 3 \times 10^{-9}$ m^2 s^{-1} selected in these computations corresponded to an aluminum-copper alloy (Reference 52, Appendix 14). The calculated solidification paths in all the cases previously presented turned out to be very close to the corresponding results based on the assumption of complete solute redistribution in the liquid. Hence, there is no reason for solving the diffusion equation in the liquid phase.

While the assumption of thermodynamic equilibrium at the solid-liquid interface during solidification applies to many industrial casting processes, at least for low solidification rates, it may lead to problems in remelting situations. This becomes particularly apparent in the Scheil limit.[33] Under the assumption of $D_s = 0$, Eq. [6] can be rewritten as

$$\frac{d\overline{w}_s}{dt} = \left(\frac{w_s^* - \overline{w}_s}{f_s}\right) \frac{df_s}{dt} \qquad [44]$$

Purposely, the value of the interfacial concentration in the solid, w_s^*, has not been replaced by the equilibrium condition (*i.e.*, $w_s^* = k\overline{w}_l$). In this particular case of no diffusion in the solid, the equilibrium condition can be used when solidification occurs (*i.e.*, when $df_s/dt > 0$) even for an open system. However, during remelting (*i.e.*, for $df_s/dt < 0$), the previously frozen profile is remelted. This has two consequences: first, a singular point (or an infinitely thin solute layer) has to be introduced at the interface in the solid in order to maintain the equilibrium condition for an open system;[33] second, the previously frozen solute profile has to be traced, which is precisely what the internal variable approach tries to avoid.[28]

A further discussion of the basic problems associated with remelting is beyond the scope of the present article. Most likely, the departure of interface equilibrium which is observed in rapid solidification (typically growth rate of the

order of m/s) should occur at much lower speed during remelting as a result of the low diffusivity in the solid (remelting rate of the order of mm/s). Therefore, even though the problem of remelting might be tracked with the transformed coordinate solution with sufficiently small meshes near the interface, the fundamental physics of remelting has to be studied in greater depth.

VI. CONCLUSIONS

A general formalism has been developed for the calculation of the solidification path once the enthalpy, $h(t)$, and solute content, $w(t)$, histories are known from the solution of the macroscopic continuity equations. This formalism accounts for the back diffusion in the solid phase, for local remelting, and for the possible eutectic formation at the end of solidification. From the known variations of $h(t)$ and $w(t)$, the local solidification path of binary alloys has been calculated according to several models:

1. an internal variable approach previously developed by Mo;[28]
2. an internal variable approach based upon a power-law approximation of the solute profile;
3. a collocation method with a third-order polynomial approximation of the solute profile; and
4. a numerical solution of the solute diffusion. A variation of this method consisted in solving also the diffusion equation in the liquid phase and in introducing the variations of solute concentrations *via* the boundary condition.

Methods 2 and 4 also have been extended to various microstructure morphologies.

The collocation method (3) and the finite-difference solution of Fick's second law (4) give solidification paths which are almost superimposed even when remelting occurs and the system is open. The collocation method offers the advantage of being more readily implemented into macrosegregation calculations. It has also been shown that the internal variable approach (1) is inferior to the power-law approximation (2).

The routine which has been developed for the solution of microsegregation is general and can incorporate any of the four models in macrosegregation calculations. It can be adapted to multicomponent alloys, at least for the primary phase solidification. Finally, it should be pointed out that the physics of remelting and the eutectic precipitation in a complex alloy system have to be studied further in order to be modeled more precisely.

ACKNOWLEDGMENTS

This research has been funded by Alusuisse-Lonza Services (Chippis); the Commission pour l'Encouragement de la Recherche Scientifique (Bern); the Office Fédéral de l'Education et de la Science (Bern); Elkem Aluminium (Norway); Hydro Aluminium (Norway); and The Research Council of Norway. The work has been carried out within the framework of the COST 512 European research collaboration, *Modelling in Materials Science and Processing.*

Appendix
Landau transformation for the solid-state diffusion

The diffusion equation which has to be solved in each phase, $\nu = s$ or l, is

$$D_\nu \frac{\partial^2 w_\nu}{\partial x^2} - \frac{\partial w_\nu}{\partial t} = 0 \qquad [A1]$$

In the solid phase, the variable domain $x \in [0, x_s(t)]$ is transformed onto a fixed domain $\varepsilon \in [1, 0]$, whereas a similar transformation can be applied to the liquid domain $[x_s(t), x_0]$ if needed. Thus, one has for the solid phase

$$\varepsilon = \frac{x}{x_s(t)} \qquad [A2]$$

The concentration field, $w_s(x, t)$, is transformed into $w_s[x(\varepsilon, t), t]$, and the new partial derivatives can be written as

$$\left[\frac{\partial w_s}{\partial x}\right]_t = \left[\frac{\partial w_s}{\partial \varepsilon}\right]_t \cdot \left[\frac{\partial \varepsilon}{\partial x}\right]_t = \frac{1}{x_s(t)} \left[\frac{\partial w_s}{\partial \varepsilon}\right]_t \qquad [A3]$$

and

$$\left[\frac{\partial w_s}{\partial t}\right]_x = \left[\frac{\partial w_s}{\partial t}\right]_\varepsilon + \left[\frac{\partial w_s}{\partial x}\right]_t \cdot \left[\frac{\partial x}{\partial t}\right]_\varepsilon = \left[\frac{\partial w_s}{\partial t}\right]_\varepsilon + \frac{\varepsilon}{x_s(t)} \left[\frac{\partial w_s}{\partial \varepsilon}\right]_t \frac{dx_s}{dt} \qquad [A4]$$

Combining Eqs. [A1] through [A4] along with the definition $x_s(t) = x_0 f_s(t)$ finally gives for the solid phase

$$\frac{D_s}{x_0^2 f_s^2} \frac{\partial^2 w_s}{\partial \varepsilon^2} - \frac{\partial w_s}{\partial t} + \frac{\varepsilon}{f_s} \frac{df_s}{dt} \frac{\partial w_s}{\partial \varepsilon} = 0 \qquad [A5]$$

REFERENCES

1. W.D. Bennon and F.P. Incropera: *Int. J. Heat Mass Transfer*, 1987, vol. 30 (10), pp. 2161-70.
2. W.D. Bennon and F.P. Incropera: *Metall. Trans. B*, 18B:611-16, 1987.
3. V.R. Voller, A.D. Brent, and C. Prakash: *Int. J. Heat Mass Transfer*, 32 (9):1719-32, 1989.
4. S. Ganesan and D.R. Poirier: *Metall. Trans. B*, 21B:173-81, 1990.
5. R. Viskanta: *JSME Int. J.*, 33 (3):409-23, 1990.
6. P.J. Prescott, F.P. Incropera, and W.D. Bennon: *Int. J. Heat Mass Transfer*, 34 (9):2351-59, 1991.
7. H. Combeau and F. Roch, I. Poitrault, J. Ch. Chevrier, and G. Lesoult: Numerical study of heat and mass transfer during solidification of steel ingots. In *Advanced Computational Methods in Heat Transfer. Vol. 3: Phase Change and Combustion Simulation*, L.C. Wrobel, C.A. Brebbia and A.J. Nowak, eds., Computational Mechanics Publications, Southampton and Boston, Co-published with Springer-Verlag, 1990, pp. 77-89.
8. F. Roch, H. Combeau, J. Ch. Chevrier, and G. Lesoult: in *Modelling of casting, welding and advanced solidification processes*, M. Rappaz, M.R. Ogzu, and K.W. Mahin, eds., TMS, Warrendale, PA, 1991, pp. 789-95.
9. J. Ni and C. Beckermann: *Metall. Trans. B*, 22B:349-61, 1991.
10. Q.Z. Diao and H.L. Tsai: *Metall. Trans. A*, 24A:963-73, 1993.
11. A. Mo: *Int. J. Heat Mass Transfer*, 36 (18):4335-40, 1993.
12. E. Haug, A. Mo, and H.J. Thevik: *Int. J. Heat Mass Transfer*, 38 (9): 1553-63, 1995.
13. A.V. Reddy and C. Beckermann: *Materials Processing in the Computer Age*, V.R. Voller, S.P. Marsh, and N. El-Kaddah, eds., TMS-AIME, Warrendale, PA, 1995, pp. 89-102.
14. H.D. Brody and M.C. Flemings: *Trans. TMS-AIME*, 1966, vol. 236, pp. 615-24.
15. T.W. Clyne and W. Kurz: *Metall. Trans. A*, 12A:965-71, 1981.

16. I. Ohnaka: *Trans. Iron Steel Inst. Jpn.*, 26:1045-51, 1986.
17. S. Kobayashi: *J. Cryst. Growth*, 88:87-96, 1988.
18. L. Nastac and D.M. Stefanescu: *Metall. Trans. A*, 24A:2107-18, 1993.
19. T.P. Battle: *Int. Mater. Rev.*, 37 (6):249-70, 1992.
20. A.J.W. Ogilvy and D.H. Kirkwood: *Appl. Sci. Res.*, 44:43-49, 1987.
21. K.S. Yeum, L. Laxmanan, and D.R. Poirier: *Metall. Trans. A*, 20A: 2847-56, 1989.
22. S. Ganesan and D.R. Poirier: *J. Cryst. Growth*, 97:851-959, 1989.
23. T.P. Battle and R.D. Pehlke: *Metall. Trans. B*, 21B:357-75, 1990.
24. V.R. Voller and S. Sundarraj: *Mater. Sci. Technol.*, 9:474-81, 1993.
25. S. Sundarraj and V.R. Voller: *Int. J. Heat Mass Transfer*, 36:713-23, 1993.
26. C.Y. Wang and C. Beckermann: *Mater. Sci. Eng.*, A171:199-211, 1993.
27. C.Y. Wang and C. Beckermann: *Metall. Trans. B*, 1993, vol. 24A, pp. 2787-2802.
28. A. Mo: *Metall. Mater. Trans. B*, 25B:597-605, 1994.
29. M.C. Schneider and C. Beckermann: *Int. J. Heat Mass Transfer*, 38(18):3455-73, 1995.
30. E.E. Emley: *Int. Met. Rev.*, 1976, June, rev. 206, pp. 75-115.
31. A. Mo, T.E. Johnsen, B.R. Henriksen, E.K. Jensen, and O.R. Myhr: in *Light Metals*, U. Mannweiler, ed., TMS-AIME, Warrendale, PA, 1994, pp. 889-96.
32. J.-M. Drezet, M. Rappaz, B. Carrupt, and M. Plata: *Metall. Mater. Trans. B*, 26B:821-829, 1995.
33. M. Rappaz and V. Voller: *Metall. Trans. A*, 21A:749-53, 1990.
34. D.R. Poirier, P.J. Nandapurkar, and S. Ganesan: *Metall. Trans. B*, 22B:889-900, 1991.
35. Daming Xu and Quigchun Li: *Num. Heat Transf.*, 20A:181-201, 1991.
36. Quiping Yu and Yaohe Zhou: *Int. J. Heat Mass Transfer*, 34(3):843-52, 1991.
37. S.D. Felicelli, J.C. Heinrich, and D.R. Poirier: *Metall. Trans. B*, 22B: 847-59, 1991.
38. *Unified Constitutive Equations*, A.K. Miller, ed., Elsevier Applied Science, New York, NY, 1987.
39. W.F. Ames: *Numerical Methods for Partial Differential Equations*, 2nd ed., Academic Press Inc., San Diego, CA, 1977.
40. W.H. Press, B.P. Flannery, S.A. Teukolsky, and W.T. Vetterling: *Numerical Recipes—The Art of Scientific Computing (FORTRAN Version)*, Cambridge University Press, Cambridge, United Kingdom, 1992.
41. H.G. Landau: *Q. Appl. Math.*, 1950, vol. 8, pp. 81-94.
42. J. Crank: *Q. J. Mech. Appl. Math.*, 10:220-31, 1957.
43. J.D. Hunt and D.J. Hebditch: *Mettal. Trans.*, 5:1557-64, 1974.
44. H. Kato and J.R. Cahoon: *Metall. Trans.*, 16A:579-87, 1985.
45. I. Vannier, H. Combeau, and G. Lesoult: *Mater. Sci. Eng.*, A173:317-21, 1993.
46. R. Mehrabian, M. Keane, and M.C. Flemings: *Metall. Trans.*, 1:1209-20, 1970.
47. M.C. Flemings and G.E. Nereo: *Trans. TMS-AIME*, 239:1449-61, 1967.
48. K.C. Chiang and H.L. Tsai: *Int. J. Heat Mass Transfer*, 35 (7):1763-70, 1992.
49. V.R. Voller and Suresh Sundarraj: *Int. J. Heat Mass Transfer*, 38 (6): 1009-18, 1995.
50. Ph. Rousset, M. Rappaz, and B. Hannart: *Metall. Mater. Trans. A*, 26A:2349-58, 1995.
51. M. Rettenmayr. Ph.D. Thesis, Max-Planck Institut für Metallforschung, Dusseldorf, Germany, 1990.
52. W. Kurz and D.J. Fisher: *Fundamentals of Solidification*, 3rd ed., Trans Tech Publication, Aedermannsdorf, Switzerland, 1992.